PIER C

(Received 4 February 2026, Accepted 25 March 2026, Scheduled 8 April 2026)

Research on Electromagnetic Interference Suppression of PMSM Position Encoder Based on Phase-Locked Loop

Chuan Xiang, Jinghao Jiao, Deyu Zhai, and Shukuan Zhang*

College of Marine Electrical Engineering, Dalian Maritime University, Dalian 116026, China

ABSTRACT: Position encoders for motors are susceptible to electromagnetic interference (EMI) in industrial environments, which distorts the position signals and degrades the motor control accuracy. This study focuses on two prevalent types of EMI: the coupling interference of switching frequency from motor drives and wideband electromagnetic background noise. To analyze their impact, a simulation platform for a permanent magnet synchronous motor (PMSM) control system was established to examine the distortion of the encoder's electrical angle signal under varying coupling voltages. A filtering suppression strategy for the position angle based on a phase-locked loop (PLL) was proposed, and its effectiveness was thoroughly analyzed. Simulation results indicate that the coupling interference of switching frequency induces periodic spike pulses in the electrical angle waveform of the encoder, whereas wideband background noise causes continuous, random fluctuations. The proposed suppression strategy demonstrates significant efficacy, achieving maximum reduction rates in electrical angle signal distortions of 80% and 80.8% for the two interference types. This method effectively mitigates the impact of electromagnetic interference on the encoder signal integrity.

1. INTRODUCTION

Permanent magnet synchronous motors (PMSMs) are characterized by high power density and efficiency, making them core drive components in high-end manufacturing, industrial robotics, and related fields [1, 2]. The accuracy of the position encoder signals, which provide critical feedback, directly determines the performance of servo control systems [3]. In precision manufacturing equipment, such as computer numerical control (CNC) machine tools and industrial robots, encoder angle errors of merely 0.1° can cause trajectory deviations exceeding tens of micrometers, severely compromising product quality. With the increasing power density of motor drives and the proliferation of wireless devices in industrial environments, electromagnetic interference has become a bottleneck limiting servo system performance.

In modern industrial settings, electromagnetic interference (EMI) is often multisource and wideband in nature. For instance, high-frequency switching devices, such as insulated-gate bipolar transistors (IGBTs), in motor drives generate switching-frequency interference typically ranging from 10 kHz to 20 kHz. This interference can infiltrate the encoder signal lines through the capacitive and inductive coupling paths [4]. Concurrently, wideband electromagnetic background noise present in the environment can be superimposed onto encoder signals via spatial radiation [5]. Both types of interference may distort the electrical angle waveform of the encoder, introduce pulse errors, and in severe cases, lead to system instability.

Substantial research has been conducted globally on EMI-suppression techniques. For example, passive common-mode filters combined with secondary periodic spread spectrum modulation have been proposed to enhance the suppression of common-mode interference [6, 7]. Active EMI filters integrated into grounding circuits have also been designed to specifically mitigate common-mode interference on the DC side of motor drives [8]. Ref. [9] introduced an active sampling strategy for nonembedded electromagnetic compatibility (EMC) uncertainty simulations. By efficiently constructing a surrogate model, it provides an advanced simulation-based evaluation method for quantifying and predicting the EMI uncertainty in complex systems. Ref. [10] presented a new technical approach to address EMI issues through the design of flexible shielding materials that primarily absorb electromagnetic waves, thereby attenuating interference at its source. Ref. [11] proposed a feedforward phase-locked loop motor position estimation method based on an embedded magnetic encoder, which effectively suppressed the impact of EMI on position detection signals. Ref. [12] describes an effective engineering practice aimed at interrupting common-mode interference currents along the transmission path, thereby significantly improving the signal integrity of encoders in complex electromagnetic environments. Ref. [13] introduced a parameter-adaptive composite active disturbance rejection control method that enhances the ability of permanent-magnet synchronous motor drive systems to suppress external electromagnetic interference. Existing research lacks the in-depth exploration and comparative analysis of the impacts of the coupling interference of switching frequency and wide-frequency background noise on motor position encoder signals. Furthermore, it has not established a unified suppression strategy to adapt to these two types of interference [14].

* Corresponding author: Shukuan Zhang (zhangshukuan@dlmu.edu.cn).

To address this gap, this study establishes a PMSM control system model incorporating a position encoder and PLL. The effects of the coupling interference of switching frequency from the motor drive and ambient wideband electromagnetic background noise on the encoder signal were comparatively analyzed under varying coupling voltages. A PLL-based position-angle filtering technique was proposed, and its suppression effectiveness against both types of interference was comprehensively evaluated.

The contributions of this study encompass systematic comparative analysis of narrowband periodic coupling interference of switching frequency versus continuous random wideband background noise effects on encoder signals, unified validation that a single PLL-based approach effectively handles both fundamentally different interference types, demonstrating strong adaptability, and establishment of quantitative evaluation metrics providing a theoretical basis for engineering parameter selection.

2. MODEL ESTABLISHMENT

2.1. Modeling of PMSM

In the three-phase stationary coordinate system, the voltage equation of a PMSM can be expressed as

$$\begin{bmatrix} u_a \\ u_b \\ u_c \end{bmatrix} = R_s \begin{bmatrix} i_a \\ i_b \\ i_c \end{bmatrix} + \frac{d}{dt} \begin{bmatrix} \psi_a \\ \psi_b \\ \psi_c \end{bmatrix} \tag{1}$$

where R_s is the stator resistance; u_a, u_b, and u_c denote the stator phase voltages; i_a, i_b, and i_c represent the corresponding phase currents; and ψ_a, ψ_b, and ψ_c are the stator flux linkages for phases a, b, and c, respectively.

By transforming the equations from the three-phase stationary coordinate system to the two-phase rotating coordinate system, the voltage equation becomes:

$$\begin{cases} u_d = R_s i_d + L_d \frac{di_d}{dt} - \omega_e L_q i_q \\ u_q = R_s i_q + L_q \frac{di_q}{dt} + \omega_e (L_d i_d + \psi_f) \end{cases} \tag{2}$$

where u_d and u_q denote the stator voltage on the dq axis; i_d and i_q are the corresponding stator currents; L_d and L_q are the inductances; ω_e is the electrical angular velocity of the motor; and ψ_f represents the permanent magnet flux linkage.

The electromagnetic torque equation is given by:

$$T_e = \frac{3}{2} P_n \left[\psi_f i_q + (L_d - L_q) i_d i_q\right] \tag{3}$$

The mechanical motion equation is given by:

$$J \frac{d\omega_m}{dt} = T_e - T_L - B\omega_m \tag{4}$$

where J is the moment of inertia, ω_m the mechanical angular velocity, T_L the load torque, and B the dampin gcoefficient.

The three-phase stationary coordinate system is transformed into a two-phase stationary system using the Clark transformation.

$$\begin{bmatrix} i_\alpha \\ i_\beta \end{bmatrix} = \frac{2}{3} \begin{bmatrix} 1 & -\frac{1}{2} & -\frac{1}{2} \\ 0 & \frac{\sqrt{3}}{2} & -\frac{\sqrt{3}}{2} \end{bmatrix} \begin{bmatrix} i_a \\ i_b \\ i_c \end{bmatrix} \tag{5}$$

where i_α and i_β are the stator current components in the $\alpha\beta$ coordinate system.

The Park transformation converts a two-phase stationary coordinate system into a two-phase rotating coordinate system.

$$\begin{bmatrix} i_d \\ i_q \end{bmatrix} = \begin{bmatrix} \cos\theta & \sin\theta \\ -\sin\theta & \cos\theta \end{bmatrix} \begin{bmatrix} i_\alpha \\ i_\beta \end{bmatrix} \tag{6}$$

where θ is the rotor electrical angle, measured by the position encoder.

2.2. Principle and Model of Motor Position Encoder under Disturbance

Figure 1 shows the working principle of an incremental photoelectric encoder, which consists of a light source, code disc, photosensitive element, and signal-conditioning circuit.

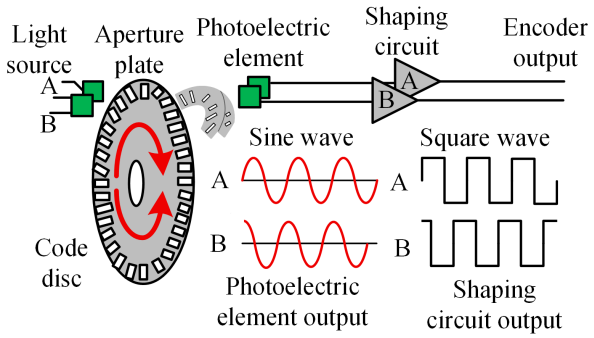

FIGURE 1. Encoder working principle.

Because the code disc rotates synchronously with the motor rotor, it allows light from the source to pass through its uniformly distributed gaps. This light was received by the photosensitive element, which converted it into two sinusoidal electrical signals, $S_A(t)$ and $S_B(t)$, with a 90° phase difference.

$$\begin{cases} S_A(t) = A \cdot \sin(\theta_m \cdot N) \\ S_B(t) = A \cdot \cos(\theta_m \cdot N) \end{cases} \tag{7}$$

where A is the signal amplitude, θ_m the mechanical angle of the rotor, and N the number of pulses per revolution.

The sinusoidal signal was converted by a comparator into the corresponding quadrature square-wave signals $A(t)$ and $B(t)$.

$$\begin{cases} A(t) = \text{sign}\left[\sin(\theta_m \cdot N)\right] \\ B(t) = \text{sign}\left[\cos(\theta_m \cdot N)\right] \end{cases} \tag{8}$$

The quadruple-frequency processing of quadrature phases A and B increases the position detection resolution by a factor of

four. The resulting pulse count, denoted as C_{quard}, yields the rotor mechanical angle θ_m as

$$\theta_m = \frac{2\pi}{4N} \cdot C_{\text{quad}} \tag{9}$$

In industrial environments, the two typical types of EMI that affect motor position encoders differ significantly in their characteristics and coupling mechanisms. Each invades the encoder signal line through distinct pathways, primarily via voltage coupling, and induces distortion in the electrical angle signal.

The coupling interference of switching frequency originating from the IGBTs in the motor drive is characterized as a narrowband periodic random pulse signal. It couples into the encoder signal line through the parasitic capacitance and inductance between the drive and encoder cables, forming an intrusive coupling voltage expressed as:

$$V(t) = \sum_k V_s \cdot e^{-\alpha\tau_k} \cdot \sin(2\pi f_s \tau_k) \cdot u(\tau_k) \tag{10}$$

where V_s is the amplitude of the coupled pulse, f_s the switching frequency, $\tau_k = t - kT_s$, and α the attenuation coefficient. In the time domain, this interference appears as a periodic spike. The discrete shift at signal zero crossings causes periodic glitches in the electrical-angle output waveform.

In industrial environments, wideband electromagnetic background noise arises from the superposition of multisource radiation emitted by devices such as frequency converters and wireless communication equipment. This noise constitutes a continuous, smooth, Gaussian random signal with a normally distributed time domain amplitude. It couples into the encoder signal line as a persistent voltage through spatial radiation and common-mode paths induced by ground potential differences and can be modeled as

$$V(t) = n(t), n(t) \sim \mathcal{N}(0, \sigma^2) \tag{11}$$

where σ^2 defines the noise power and is positively correlated with the coupling voltage strength. This interference exhibited continuous random fluctuations in the time domain. The random variations at signal zero-crossings introduce sustained randomness into the output electrical angle.

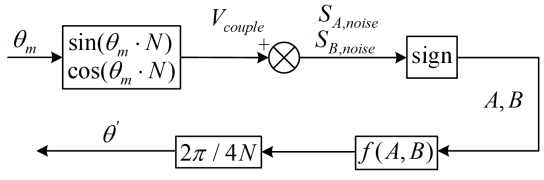

FIGURE 2. Position encoder system model.

The model of the position encoder system is shown in Figure 2. Assuming an interference coupling voltage $V_{\text{couple}}(t)$, the disturbed sinusoidal signal becomes

$$\begin{cases} S_{A,\text{noise}}(t) = S_A(t) + V_{\text{couple}}(t) \\ S_{B,\text{noise}}(t) = S_B(t) + V_{\text{couple}}(t) \end{cases} \tag{12}$$

The interfered signals $S_{A,\text{noise}}(t)$ and $S_{B,\text{noise}}(t)$ are converted by a comparator, which toggles at the zero-crossing of the signal. The superimposed interference voltage shifts the actual zero-crossing points, thereby advancing or delaying the edges of the resulting square waves $A(t)$ and $B(t)$. This introduces a phase jitter and pulse-width distortion.

After the frequency multiplication and pulse counting of the disturbed square wave, the resulting mechanical angle θ'_m accumulates an error $\Delta\theta_m(t)$ originating from the zero-crossing shift.

$$\theta'_m(t) = \theta_{m,\text{ideal}}(t) + \Delta\theta_m(t) \tag{13}$$

2.3. Principle and Model of Position Angle Filtering for PLL

As a closed-loop controller for phase tracking and signal purification, the PLL locks to the fundamental phase of a noisy input angle signal by dynamically adjusting its output. With the encoder's noisy signal as the input, the PLL utilizes phase detection, error filtering, and dynamic correction to make its estimated phase track the input in real time. This process inherently attenuates high-frequency spikes and random fluctuations, thereby suppressing both the switching-frequency coupling and wideband electromagnetic noise. Its structure is illustrated in Figure 3.

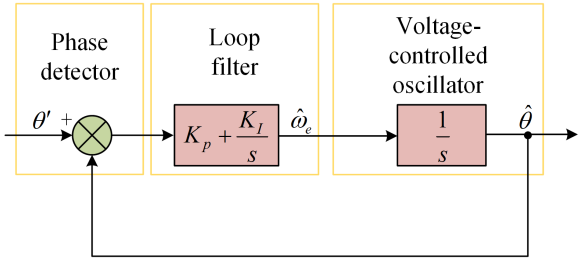

FIGURE 3. PLL working principle.

Structurally, a basic PLL is composed of three core components: a phase detector, a loop filter, and a voltage-controlled oscillator.

The phase deviation between the input electrical angle and its estimated value is obtained using a phase detector. First, the encoder output is transformed into orthogonal components via the Clark transformation. A quadrature multiplier then processes these components to extract the deviation, yielding the following error signal

$$e = -\sin\hat{\theta} \cdot \lambda_1 + \cos\hat{\theta} \cdot \lambda_2 \tag{14}$$

where $\hat{\theta}$ is the phase-estimation value.

The loop filter employs a proportional-integral (PI) controller structure to smooth the error signal and eliminate steady-state deviation, leveraging both proportional and integral actions. Its transfer function is

$$F(s) = K_p + \frac{K_i}{s} \tag{15}$$

where K_p is the proportional gain, and K_i is the integral gain.

Acting as a phase-adjustment actuator, the voltage-controlled oscillator updates its output phase estimate $\hat{\theta}$ based

on the control signal from the loop filter. The rate of change of $\hat{\theta}$ is proportional to this control signal, as expressed by

$$\hat{\theta}(t) = \hat{\theta}_0 + \int_0^t u(\tau)d\tau \tag{16}$$

where $\hat{\theta}_0$ is the initial phase estimation value.

2.4. System Model and Parameters

The PMSM under study has the following parameters: rated power 3 kW; stator resistance $R_s = 1.5\,\Omega$; dq-axis inductance $L_d = L_q = 0.0059$ H; rotational inertia $J = 0.003\,\text{kg}\cdot\text{m}^2$; damping coefficient $B = 0.008\,\text{N}\cdot\text{m}\cdot\text{s/rad}$; pole pairs $p = 4$; and DC bus voltage 311 V. The corresponding simulation model of the PMSM control system is illustrated in Figure 4.

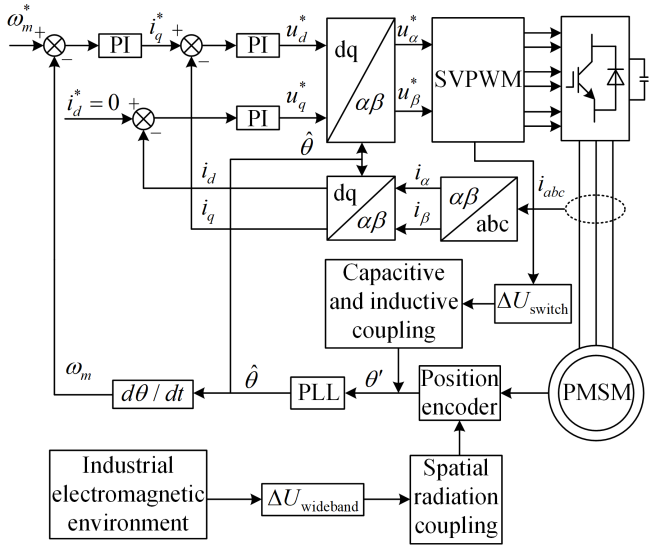

FIGURE 4. Simulation model of the PMSM control system.

The speed loop and current loop proportional-integral (PI) controllers are tuned using the conventional engineering design method for PMSM servo systems. The current loop is designed with a bandwidth of 1000 Hz to ensure rapid current tracking, with proportional gain $k_{p\_i} = 300$ and integral gain $k_{i\_i} = 2395$. The speed loop is configured with a bandwidth of 100 Hz to maintain stable speed regulation, with proportional gain $k_{p\_\omega} = 0.2$ and integral gain $k_{i\_\omega} = 30$. These parameters are determined through pole placement techniques, ensuring adequate phase margin and gain margin.

3. RESEARCH ON THE IMPACT OF EMI ON POSITION ENCODERS

This study aims to elucidate the mechanism by which EMI deteriorates position encoder signal performance. It investigates the differential impact of two typical interference types, switching-frequency coupling from motor drives and wideband electromagnetic background noise in industrial environments, on the waveform characteristics, key parameter evolution, and distortion of the encoder's electrical angle signal. Quantitative analysis clarified the distinct effects of these two interference types.

3.1. Influence Law of Coupling Interference on Switching Frequency

In accordance with IEC 61000-6-2:2016, five coupling voltage levels, 0.1 V, 0.5 V, 1.0 V, 2.0 V, and 3.0 V are selected to span low, medium, and high interference scenarios, with the parameters $f_s = 10$ kHz matching the inverter switching frequency and $\alpha = 5000\,\text{s}^{-1}$ determined from typical cable parasitic parameter values. This voltage is superimposed onto the ideal sinusoidal encoder signals $S_A(t)$ and $S_B(t)$ through a summation junction immediately after the signal generation stage, simulating capacitive and inductive coupling from adjacent power cables. The resulting electrical angle distortion was examined in terms of the waveform morphology, quantized parameters, and their variation patterns.

Figure 5 depicts the electrical angle waveform of the encoder under motor drive the coupling interference of switching frequency at various coupling voltages. At a low voltage 0.1 V, the waveform remains a smooth sawtooth with periodic, sparse spikes occurring at switching instants because the interference energy is insufficient to exceed the encoder's noise margin. When the voltage increases to 1.0 V, the spikes overlap at switching harmonics, amplifying the capacitive coupling effect and distorting the signal timing. At 3.0 V, the waveform was dominated by dense spikes. Capacitive coupling induces spikes that are sufficiently large to cause logic-level misjudgment, resulting in complete signal misalignment.

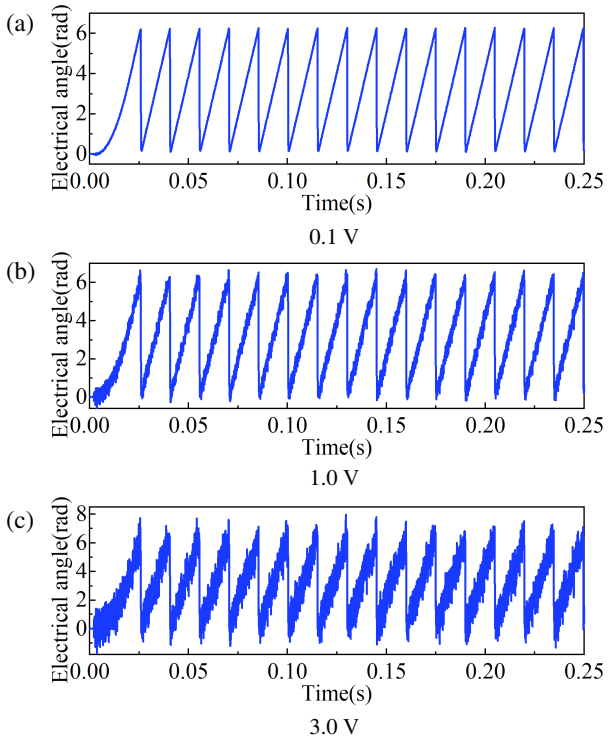

FIGURE 5. Electrical angle waveforms under different interference intensities.

Figure 6 illustrates the evolution of the key signal characteristics under the coupling interference of switching frequency. As shown in Figure 6(a), phase jitter increases nonlinearly from 0.08 rad to 1.16 rad with rising voltage, a trend driven by the

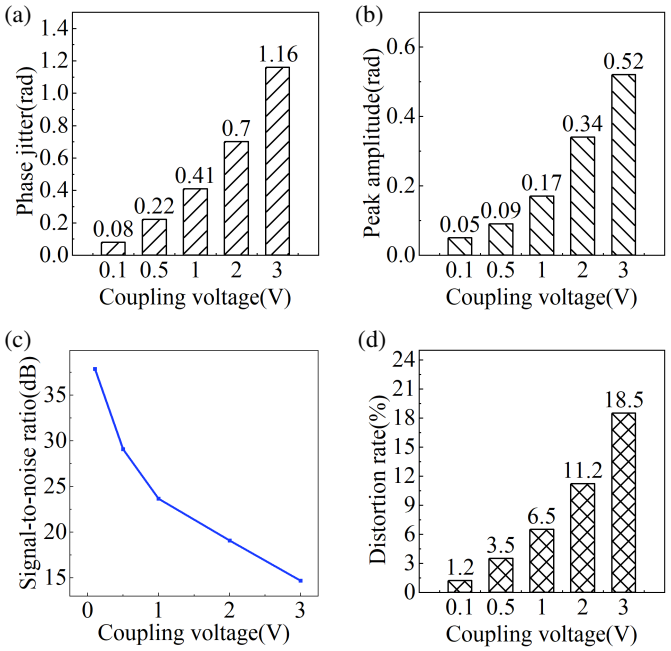

FIGURE 6. Key characteristics of electrical angle signals under the coupling interference of switching frequency. (a) Relationship between the phase jitter and coupling voltage. (b) Relationship between the peak amplitude and coupling voltage. (c) Relationship of signal-to-noise ratio and coupling voltage. (d) Relationship of distortion rate and coupling voltage.

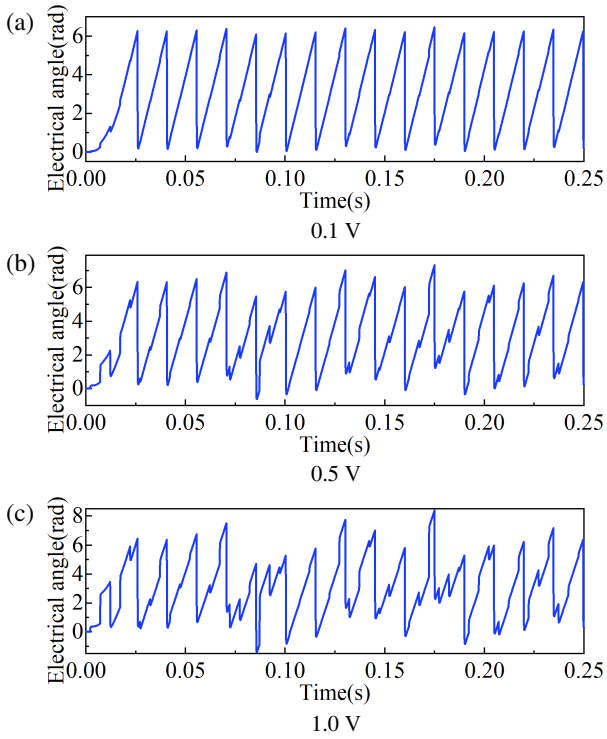

FIGURE 7. Electrical angle waveforms under different interference intensities.

quadratic growth of pulse energy. Figure 6(b) shows that the peak amplitude rises linearly from 0.05 rad to 0.52 rad over the same range. Concurrently, the signal-to-noise ratio decays rapidly from 37.9 dB to 14.7 dB, as presented in Figure 6(c), while the distortion rate climbs from 1.2% to 18.5%, detailed in Figure 6(d). These trends collectively reveal pronounced nonlinear degradation and indicate a voltage threshold beyond which signal distortion escalates sharply.

3.2. The Influence Pattern of Wideband Electromagnetic Noise

In accordance with CISPR 16-2-3:2016 and the electromagnetic disturbance limits for industrial environments, five coupling voltage levels 0.05 V, 0.1 V, 0.2 V, 0.5 V, and 1.0 V are selected to represent a practical range of interference intensities. Gaussian white noise with zero mean and variance σ^2 proportional to the coupling voltage level is generated using the band-limited white noise block with sampling time 1 μs, then filtered through a 10 MHz low-pass filter to represent the bandwidth-limited nature of spatial radiation coupling. The resulting electrical angle distortion was examined in terms of the waveform characteristics, quantized parameters, and their variation trends.

Figure 7 illustrates the electrical angle waveform of the position encoder under wideband electromagnetic background noise at different coupling voltages. At 0.1 V, the waveform appears largely unaffected, maintaining a periodic sawtooth profile with only minor spikes at discrete noise frequencies because the interference energy remains below the encoder's noise margin. When the voltage rises to 0.5 V, spikes overlapped across multiple frequency bands, intensifying the electromagnetic coupling effect. This significantly degrades the waveform smoothness and distorts the signal timing. At 1.0 V, the signal was dominated by dense interference clutter. The superposition of high-frequency spikes severely degrades the measurement accuracy, causing edge misjudgment and rendering the encoder output unusable for reliable positional feedback.

Figure 8 depicts the evolution of the key signal characteristics under wideband electromagnetic background noise. As shown in Figure 8(a), phase jitter increases tenfold from 0.04 rad to 0.4 rad due to the exponential growth of noise energy, while Figure 8(b) indicates a linear rise in maximum fluctuation amplitude, reflecting cumulative interference. The signal-to-noise ratio decays from 41.9 dB to 19.4 dB as shown in Figure 8(c), and the distortion rate increased from 1.5% to 21.3%, as shown in Figure 8(d). These trends confirm a distinct voltage threshold effect, beyond which distortion sharply escalates a continuous degradation mechanism that differs from the periodic distortion induced by switching-frequency coupling.

3.3. Verification of Interference Mechanism Analysis

This section validates the two types of interference mechanisms proposed in Section 2.2 through simulation analysis. By comparing the electrical angle waveform characteristics (Figure 5 and Figure 7) and parameter evolution laws (Figure 6 and Figure 8) of the coupling interference of switching frequency and wideband background noise under different coupling voltages, the essential differences between the two types of interference are verified.

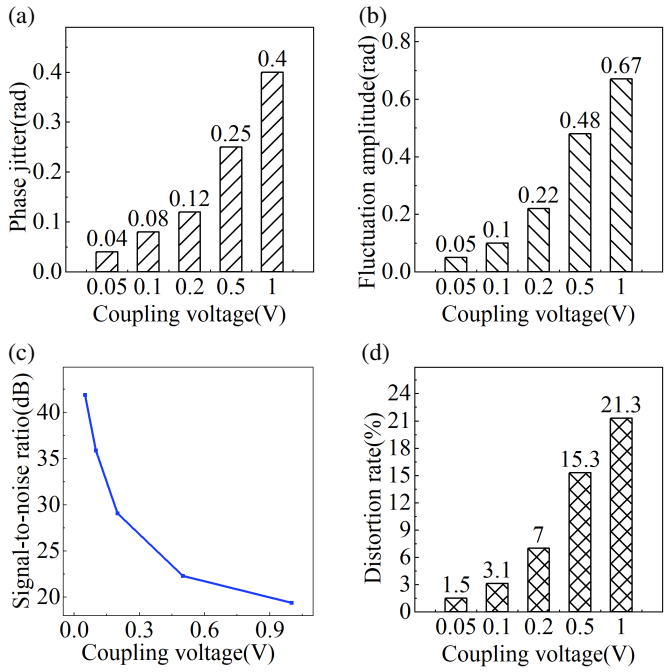

FIGURE 8. Key parameter characteristics of electrical angle signals under wideband electromagnetic background noise. (a) Relationship of phase jitter and coupling voltage. (b) Relationship of fluctuation amplitude and coupling voltage. (c) Relationship of signal-to-noise ratio and coupling voltage. (d) Relationship of distortion rate and coupling voltage.

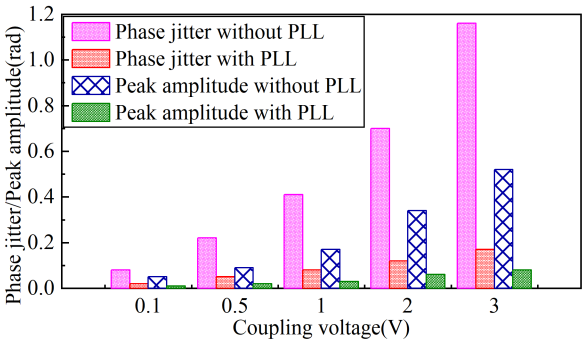

FIGURE 9. Comparison of phase jitter and peak amplitudes of electrical angle signals with and without PLL.

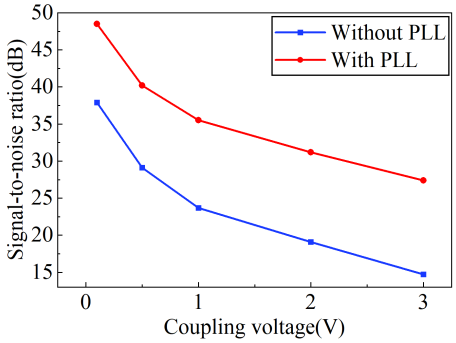

FIGURE 10. Comparison of signal-to-noise ratios of electrical angle signals with and without PLL.

Figure 5 shows that the waveform exhibits periodic spikes synchronized with the switching period, verifying the mechanism of periodic glitches caused by discrete shift in the coupling interference of switching frequency described in Section 2.2. Figure 7 demonstrates that the waveform exhibits continuous random fluctuation characteristics, verifying the mechanism of continuous randomness in wideband electromagnetic noise described in Section 2.2.

For the coupling interference of switching frequency, the phase jitter in Figure 6 increases nonlinearly from 0.08 rad to 1.16 rad, reflecting the quadratic growth characteristic of pulse energy, which is consistent with the prediction of pulse energy increasing with the square of coupling voltage. For wideband background noise, the phase jitter increased from 0.04 rad to 0.4 rad, reflecting the exponential growth characteristic of noise energy.

4. RESEARCH ON THE SUPPRESSION EFFECT OF EMI BASED ON PLL

Under the influence of five sets of coupled voltages from two types of interference, the suppression effect was investigated using PLL filtering technology.

4.1. Suppression Effect of Switching Frequency Coupling Interference

Given the narrowband periodic-pulse nature of the coupling interference of switching frequency, we employed a PLL to capitalize on its phase-tracking and high-frequency suppression capabilities. The suppression effect was evaluated through quantitative analysis of key waveform parameters.

Figure 9 compares the phase jitter and spike amplitudes of the electrical angle signal of the encoder with and without PLL suppression under varying coupling voltages. Without the PLL, both parameters increase significantly — phase jitter from 0.08 rad to 1.16 rad and spike amplitude from 0.05 rad to 0.52 rad — due to the escalating conducted coupling of switching-frequency harmonics. With the PLL, they are dramatically reduced: phase jitter is suppressed to between 0.02 rad and 0.17 rad, and spike amplitude to between 0.01 rad and 0.08 rad, demonstrating stable and effective suppression across the entire voltage range and verifying the PLL's capability against this interference.

Figure 10 illustrates the signal-to-noise ratios of the electrical angle signal of the encoder under the coupling interference of switching frequency with and without PLL filtering. Without the PLL, the signal-to-noise ratio deteriorates markedly from 37.9 dB to 14.7 dB as the coupling voltage increases from 0.1 V to 3.0 V, due to the accumulating energy of switching harmonics. In contrast, with PLL filtering, the signal-to-noise ratio is maintained at a high level — 48.5 dB at 0.1 V and 27.4 dB at 3.0 V. It demonstrates the effectiveness of the PLL in mitigating interference and significantly improving signal purity.

Figure 11 illustrates the distortion rates of the encoder's electrical angle signal with and without a PLL under the coupling interference of switching frequency. Without the PLL, the distortion rate increases nonlinearly from 1.2% to 18.5% as the coupling voltage rises from 0.1 V to 3.0 V. With the PLL, the

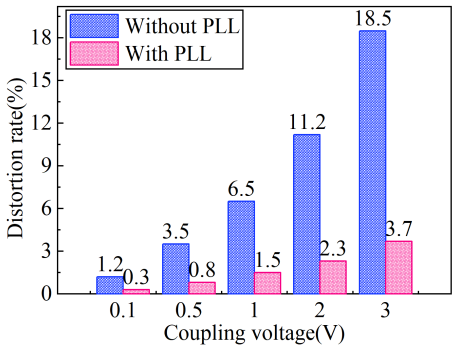

FIGURE 11. Comparison of distortion rates of electrical angle signals with and without PLL.

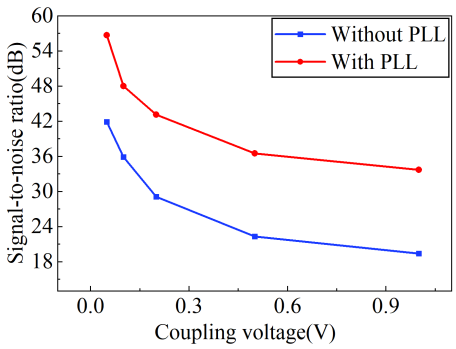

FIGURE 13. Comparison of signal-to-noise ratios of electrical angle signals with and without PLL.

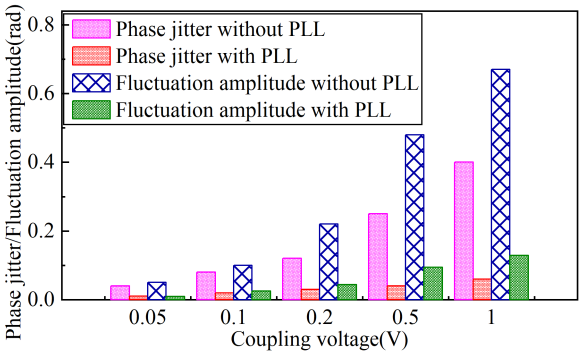

FIGURE 12. Comparison of phase jitter and fluctuation amplitudes of electrical angle signals with and without PLL.

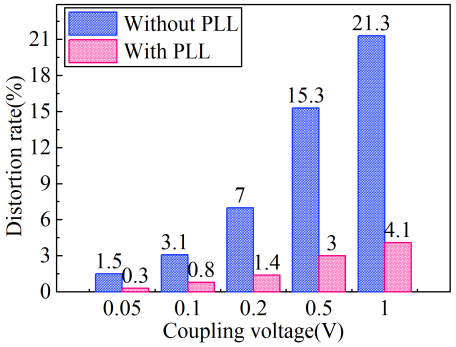

FIGURE 14. Comparison of distortion rates of electrical angle signals with and without PLL.

distortion is notably suppressed, reaching only 0.3%, 0.8%, 1.5%, 2.3%, and 3.7% at the respective voltage levels. This corresponds to a maximum suppression rate of 80%, demonstrating the effectiveness of the PLL in mitigating waveform distortions and ensuring accurate position detection.

4.2. Suppression Effect of Wideband Electromagnetic Noise

Given the continuous spectrum and persistent random fluctuations of wideband electromagnetic background noise, this study focuses on the fundamental-wave tracking and clutter rejection capabilities to evaluate its efficacy in suppressing this type of interference.

Figure 12 compares the phase jitter and fluctuation amplitudes of the electrical angle signal of the encoder with and without the PLL under wideband electromagnetic noise. Without the PLL, both parameters increase with the coupling voltage owing to the continuous noise intrusion and energy accumulation via spatial radiation. With the PLL, the phase jitter is confined to 0.01–0.06 rad and the fluctuation amplitude to 0.009–0.129 rad, achieving suppression rates exceeding 75% and 82%, respectively. These results demonstrate that PLL significantly enhances both the timing and amplitude stability of the signal.

Figure 13 illustrates the variation in the signal-to-noise ratios of the electrical angle signal of the encoder with and without the PLL. Without the PLL, the signal-to-noise ratio collapses from 41.9 dB at 0.05 V to 19.4 dB at 1.0 V due to the accumulating energy of wideband interference. With the PLL, the signal-to-noise ratio was sustained at a significantly higher level, showing an improvement of 12.1 to 15.0 dB across the voltage range. This demonstrates the excellent suppression capability of the PLL against the wideband electromagnetic background noise.

Figure 14 presents the distortion rates of the electrical angle signal of the encoder with and without the PLL under wideband electromagnetic noise. Without the PLL, the distortion rate increases nonlinearly from 1.5% to 21.3% as the coupling voltage rises from 0.05 V to 1.0 V, reflecting the signal's degradation under continuous spectrum interference. With the PLL, the distortion rates were markedly reduced to 0.3%, 0.8%, 1.4%, 3.0%, and 4.1% at the corresponding voltages, achieving a maximum suppression of 80.8%. These results confirm the effectiveness of the PLL in mitigating waveform distortion and ensuring angle detection accuracy.

4.3. Comparison of Hardware and Software EMI Suppression Approaches

Compared to hardware design approaches that are more commonly employed in engineering practice, this paper proposes a software method based on a Phase Locked Loop (PLL) for electromagnetic interference suppression. Hardware approaches to suppress electromagnetic interference in position encoder systems primarily include shielding, filtering, grounding, and active filters. The fixed parameters of these hardware methods render them inflexible and unable to adapt to changing inter-

TABLE 1. Comparison of hardware and software EMI suppression approaches.

	Hardware approach	PLL-based software approach
Implementation Cost	Medium-High	Low
Space Requirement	Significant	Negligible
Real-time Response	Immediate	Minimal delay
Reliability in Extreme Environments	High	Dependent on controller stability
Effectiveness for High-intensity Interference	Strong	Limited
Adaptability	Fixed characteristics; difficult to modify post-installation	Parameter-tunable; adaptable to varying interference types

ference environments. Moreover, the additional components required increase system volume and cost, and the physical components are subject to degradation and failure, necessitating regular maintenance. In contrast, the PLL-based software approach offers distinct advantages by dynamically estimating and compensating for phase errors introduced by interference through its closed-loop tracking mechanism. It requires no additional physical components as it can be implemented entirely within existing controller firmware, thereby overcoming the space, cost, and flexibility constraints inherent to hardware based solutions. Table 1 presents a comparison of hardware and software EMI suppression methods.

Hardware methods excel as the foundational protective barrier, physically preventing interference from entering the signal chain. Their superiority lies in handling high-intensity interference, ensuring reliability in safety-critical systems. Software methods, including PLL-based filtering, serve most effectively as supplementary refinement mechanisms that enhance signal quality when hardware alone proves insufficient or when physical modification is impractical. The most robust industrial implementations typically employ hybrid architectures, where hardware suppresses most of the interference, and software algorithms address residual disturbances and adaptive compensation requirements.

4.4. Limitations and Future Work

EMI is essentially a physical phenomenon involving complex coupling paths, parasitic parameters, and environmental variations. This study is based on simulation models that involve some idealized assumptions, including interference characteristics, simplified lumped parameter coupling models, etc. These simplifications may not fully represent the complexity of actual industrial electromagnetic environments, as in real environments, factors such as the actual cable routing geometry, frequency-dependent shielding effectiveness, grounding impedance variations, and multipath interference superposition effects all play significant roles.

Future work will focus on experimental validation through the construction of a hardware-in-the-loop test platform with programmable interference injection and comparative evaluation using commercial encoders in controlled electromagnetic environments.

5. CONCLUSION

This study established a PMSM control system model incorporating an encoder and a phase-locked loop to address electromagnetic interference issues. The mechanisms of two typical EMI types were investigated: switching-frequency coupling introduces periodic spikes with nonlinear distortion growth, whereas wideband background noise causes continuous random fluctuations. The proposed PLL-based filtering strategy effectively suppressed both interference types via closed-loop control, achieving maximum distortion reduction rates of 80% and 80.8%, respectively. The contributions of this paper are established at the theoretical and simulation validation level, providing foundational support for the PLL filtering method in electromagnetic interference suppression for PMSM position encoders. Nevertheless, comprehensive validation necessitates future experiment verification to address physical non-idealities, including actual coupling path characteristics, parasitic parameters, and environmental variability.

ACKNOWLEDGEMENT

This work was supported by the National Key Research and Development Program of China (Grant Number 2023YFB4301500).

REFERENCES

[1] Rafaq, M. S., W. Midgley, and T. Steffen, "A review of the state of the art of torque ripple minimization techniques for permanent magnet synchronous motors," *IEEE Transactions on Industrial Informatics*, Vol. 20, No. 1, 1019–1031, 2024.

[2] Song, W., J. Li, C. Ma, Y. Xia, and B. Yu, "A simple tuning method of PI regulators in FOC for PMSM drives based on deadbeat predictive conception," *IEEE Transactions on Transportation Electrification*, Vol. 10, No. 4, 9852–9863, 2024.

[3] Zhang, X., Y. Chen, and X. Sun, "Overview of active disturbance rejection control for permanent magnet synchronous motors," *Journal of Electrical Engineering & Technology*, Vol. 19, No. 3, 1237–1255, 2024.

[4] Wang, L., L. Yu, A. Han, and Z. Shi, "A novel phase current difference construction based initial rotor position detection method for surface mounted pmsm without injections of high-frequency voltage or pulse sequence," *Journal of Electrical Engineering & Technology*, Vol. 19, No. 7, 4369–4380, 2024.

[5] Kalaiarasu, S. and S. Natarajan, "Conducted electromagnetic interference mitigation on two-stage cascaded boost (TSCB) DC-DC converter using FPGA based DCPWM technique for EV Applications," *Journal of Electrical Engineering & Technology*, Vol. 18, No. 3, 2003–2013, 2023.

[6] Li, D., X. Hu, B. Gao, W.-Y. Yin, H. Chen, and H. Qian, "Highly transparent tunable microwave perfect absorption for broadband microwave shielding," *Progress In Electromagnetics Research*, Vol. 176, 35–44, 2023.

[7] Xiao, J. and W. Yang, "Study of a common mode passive filter combined with secondary periodic spread spectrum," *Journal of Electrical Engineering & Technology*, Vol. 20, No. 5, 3279–3289, 2025.

[8] Chai, J., W. Wang, and T. Liu, "Discontinuous PWM-based common-mode voltage suppression method for three-phase inverter," *Journal of Power Electronics*, Vol. 25, No. 2, 250–259, 2025.

[9] Zhang, Y. and D. Jiang, "An active EMI filter in grounding circuit for DC side CM EMI suppression in motor drive system," *IEEE Transactions on Power Electronics*, Vol. 37, No. 3, 2983–2992, 2022.

[10] Bai, J., J. Wang, X. Ji, Y. Song, and H. Cao, "Active sampling strategies for non-embedded EMC uncertainty simulation," *Progress In Electromagnetics Research C*, Vol. 160, 29–38, 2025.

[11] Mishra, H., N. Negi, V. Rathi, B. Prasad, and V. Mishra, "Investigation of electromagnetic interference shielding properties in PVDF-PVP composite films reinforced with VGCNF," *Progress In Electromagnetics Research C*, Vol. 154, 139–145, 2025.

[12] Wang, Y., H. Ahmed, H. Zhang, and W. Hua, "Feedforward PLLs for motor position estimation using embedded magnetic encoder," *IEEE Sensors Journal*, Vol. 24, No. 7, 10 307–10 315, 2024.

[13] Xiang, C., Y. Nan, H. Shi, Y. Zhang, and S. Zhang, "Research on the anti-electromagnetic interference performance of motor position encoder by cable grounding method," *Progress In Electromagnetics Research C*, Vol. 161, 246–254, 2025.

[14] Huang, Y., Y. Xie, W. Han, and L. Ling, "Parameter-adaptive composite active disturbance rejection control for permanent magnet synchronous motor drives," *Progress In Electromagnetics Research B*, Vol. 114, 13–25, 2025.